Simulation study on X-ray phase contrast imaging with Dual-Phase Gratings

Johannes Bopp · Veronika Ludwig · Maria Seifert · Georg Pelzer · Andreas Maier · Gisela Anton · Christian Riess

Abstract *Purpose:* Two phase gratings in an X-ray grating interferometers can solve several technical challenges for clinical use of X-ray phase contrast. In this work, we adapt and evaluate this setup design to clinical X-ray sources and detectors in a simulation study.

Methods: For a given set of gratings, we optimize the remaining parameter space of a Dual-Phase Grating setup using a numerical wave front simulation. The simulation results are validated with experimentally obtained visibility measurements on a setup with a microfocus tube and a clinical X-ray detector. We then confirm by simulation that the Lau condition for the G_0 grating also holds for two phase gratings. Furthermore, we use a G_0 grating with a fixed period to search for periods of matching phase grating configurations.

Results: Simulated and experimental visibilities agree very well. We show that the Lau condition for a Dual-Phase Grating setup requires the interference patterns of the first phase grating to constructively overlay at the second phase grating. Furthermore, a total of three setup variants for given G_0 periods were designed with the simulation, resulting in visibilities between 4.5 % and 9.1 %.

Conclusion: Dual-Phase gratings can be used and optimized for a medical X-ray source and detector. The obtained visibilities are somewhat lower than

J. Bopp (✉) · C. Riess · A. Maier
Pattern Recognition Lab
Martensstr. 3
91058 Erlangen
Germany
Tel.: +49-9131-85-27775
Fax: +49-9131-85-27270
E-mail: Johannes.Bopp@fau.de

V. Ludwig · M. Seifert · G. Pelzer · G. Anton
ECAP
Erwin-Rommel-Str. 1
91058 Erlangen
Germany

for other Talbot-Lau interferometers, and are a tradeoff between setup length and spatial resolution (or additional phase stepping, respectively). However, these disadvantage appears minor compared to the overall better photon statistics, and the fact that Dual-Phase Grating setups can be expected to scale to higher X-ray energies.

Keywords Phase contrast imaging, Talbot-Lau, Grating based interferometry, Dual-Phase Grating

1 Introduction

Bonse and Hart proposed the first phase-sensitive X-ray system in 1965 [1]. Since then, several phase-sensitive setups have been proposed. The phase signal can in principle provide superior contrast for materials with low atomic numbers such as soft-tissue [2]. Endrizzi provides an overview of various phase-sensitive X-ray setups that have been proposed since then [3]. Among these possibilities, the Talbot-Lau interferometer (TLI) is a promising design for translation into the hospital due to its compatibility with clinical X-ray equipment [4]. It consists of three gratings between X-ray source and detector, and provides the three signals absorption, differential phase shift, and dark-field.

The phase and dark-field signals are complementary to the traditional X-ray absorption. Phase and dark-field lead to several promising results in preclinical medical studies and in non-destructive testing. For example, the high soft tissue contrast of the phase can aid mass detection in mammography . The dark-field can support detection of micro calcifications in female breasts [5,6], detection of foreign bodies [7] and cartilage diagnostics [8]. Dark-field also showed very promising results for lung imaging: it can visualize density differences between soft tissue and air at the pulmonary alvioli, which allows to detect several lung diseases. The reported detectabilities of pulmonary emphysema [9], pulmonary fibrosis [10], and lung cancer [11] are much higher than in traditional absorption imaging.

However, TLI has still to overcome some challenges towards its clinical use. Particularly, the last of the three TLI gratings, G_2, poses multiple difficulties. First, G_2 absorbs 50 % of the photons behind the ~~patient~~ sample, which effectively doubles the radiation dose. Second, and more importantly, manufacturing grating G_2 with an aspect ratio large enough to absorb higher X-ray energies is a hard problem [12,13]. This is the main hindrance towards building high energy setups [14, 15]. As a consequence, a setup design that allows to omit G_2 both halves the radiation dose and allows to image larger and denser specimen.

Recently, Miao *et al.* and Kagias *et al.* proposed a PCI setup design where the G_2 grating is replaced by a second phase grating G_1' [16,17]. A sketch of such a setup is shown in Fig. 1b. However, Miao *et al.* and Kagias *et al.* only showed proof-of-concept experiments with parameters that are quite different from potential clinical requirements.
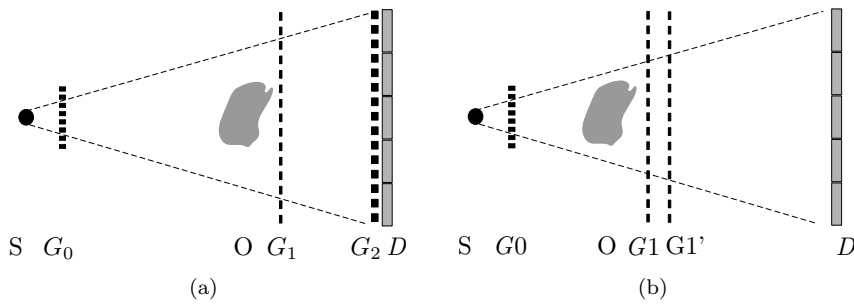
Fig. 1: Schematic view of the traditional Talbot-Lau X-ray interferometer (left) and the novel Dual-Phase Grating Interferometer (right).

In this work, we take several important steps towards translating the idea of two phase gratings to more realistic clinical parameters. First, we report experimental measurements and simulations on grating periods that can be reliably produced, using a detector with a point spread function (PSF) that is comparable to a clinical system. Then we use simulations to verify an adapted version of the Lau condition for the Dual-Phase Grating interferometer. This enables the use of a clinical X-ray source with a large focal spot and much larger flux. Third, we show how to effectively design specific Dual-Phase Grating setups by performing an example optimization for a range of grating periods. This paper is a substantial extension of earlier works [18,19], as it includes a G_0 grating to allow the use of typical clinical X-ray sources.

2 Material and Methods

2.1 Talbot-Lau Interferometer and Dual-Phase Grating Interferometer

A typical X-ray Talbot-Lau Interferometer consists of three gratings G_0, G_1, G_2 (see Fig. 1a). G_1 periodically modulates the phase of a coherent wave. Due to the Talbot effect, the grating pattern reappears downstream at Talbot distances as self image in the intensity values [20]. Phase shifts by objects cause a shift of the intensity pattern at the detector.

The intensity pattern is typically much finer than a detector pixel. Thus, an absorption grating G_2 is used to sample the signal. The signal is then reconstructed either from phase stepping, i.e., multiple acquisitions with a laterally moving G_2, or single-shot Moiré imaging [21,22]. Grating G_0 splits the source in multiple laterally coherent, but mutually incoherent line sources, which allows the use of medical X-ray tubes with a large focal spot.

For reconstruction of attenuation, differential phase and dark-field, a sine curve is fitted to the measurements for each pixel,

$$I(x) = I_0 \left[1 + v \sin \left(\frac{2\pi}{p_2} x + \phi \right) \right] \ . \tag{1}$$

Here, I_0 denotes the mean intensity (corresponding to absorption), ϕ is the differential phase, and p_2 the period of grating G_2. The amplitude v is also known as visibility, and is the basis for computing the dark-field signal. It can be calculated from phase-stepping or Moiré fringes as

$$v = \frac{\max(I(x)) - \min(I(x))}{\max(I(x)) + \min(I(x))} \ . \tag{2}$$

Visibility is also the primary figure of merit for optimizing the interferometer design, as it describes the signal strength relative to the overall intensity.

Replacing the absorption grating G_2 with a second phase grating G_1' leads to the *Dual-Phase Grating Interferometer* (see Fig. 1b), which has several advantages. First, the height of the phase grating G_1' is much lower than the height of the absorption grating G_2. Hence, it is considerably easier to fabricate, and scales better to medically relevant X-ray energies of about $100\,\mathrm{keV}$. Second, G_2 always absorbs half of the photons behind the ~~patient~~ sample, thereby reducing the photon efficiency of the system. Conversely, the phase grating G_1' is mostly transparent. ~~More importantly, can be installed in front of the patient, thereby avoiding any post-patient photon absorption.~~

The key idea is to choose the periods of G_1 and G_1' with similar size, such that the combined wave has a low-frequency Moiré pattern that can be directly resolved by the detector. More specifically, the effect of the two phase gratings onto wave Φ is modeled as

$$
\Phi \left[\overbrace{\cos\left(\frac{2\pi x}{p_1^{\mathrm{proj}}}\right)}^{G1 \text{ projected onto } G1'} + \overbrace{\cos\left(\frac{2\pi x}{p_1'}\right)}^{G_1'} \right]
$$
$$
= 2\Phi \underbrace{\cos\left[\pi x \left(\frac{1}{p_1^{\mathrm{proj}}} - \frac{1}{p_1'}\right)\right]}_{\text{Moiré pattern}} \underbrace{\cos\left[\pi x \left(\frac{1}{p_1^{\mathrm{proj}}} + \frac{1}{p_1'}\right)\right]}_{\text{high frequency part}} , \tag{3}
$$

where p_1 and p_1' denote the period of gratings G_1 and G_1', and p_1^{proj} is the projection of p_1 onto G_1'. The magnification of p_1 on G_1' is calculated with the intercept theorem as

$$p_1^{\mathrm{proj}} = \frac{\mathrm{d}(S, G_1')}{\mathrm{d}(S, G_1)} \cdot p_1 \ , \tag{4}$$

where $\mathrm{d}(S, G_1)$ and $\mathrm{d}(S, G_1')$ denote the distances between source S and grating G_1 and source S and grating G_1', respectively.

Equation 3 states that the combined wave can be decomposed into a higher and a lower frequency component. We refer to the lower frequency component as the envelope. To design a system without G_2 grating, the goal is to choose the low frequency in the order of magnitude of the detector pixels, while the high-frequency part must be large enough to vanish in the detector signal. In
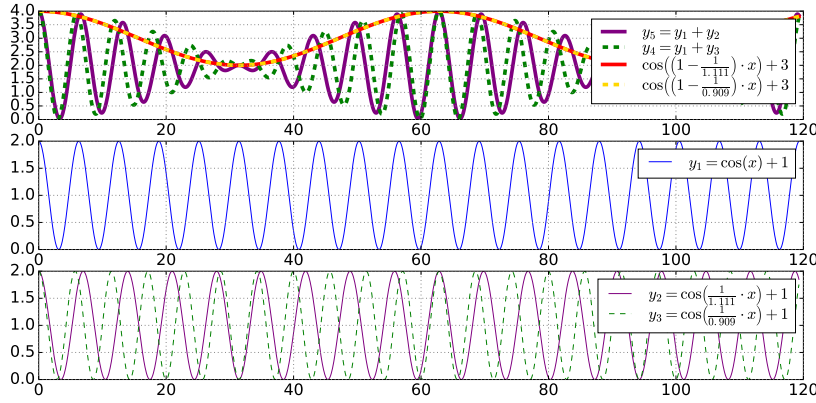
Fig. 2: Example envelope construction from a wave modulation at G_1' and a wave modulation at G_1 projected onto G_1'. Top: two identical low-frequency envelopes (orange, yellow) with varying high-frequency components (dashed green, purple). Middle: wave modulation at G_1' grating. Bottom: two wave modulations of G_1 projected onto G_1' that create identical envelopes.

practice, both requirements can be well addressed. The low-frequency period is

$$p_b = \frac{1}{\text{abs}\left(\frac{1}{p_1^{\text{proj}}} - \frac{1}{p_1'}\right)} \ , \tag{5}$$

at G_1', and is further magnified along the propagation distance between G_1' and the detector. For a given p_1', there are always two solutions for p_1^{proj} to create the same envelope due to the absolute difference in the denominator of Eqn. 5. This is illustrated in Fig. 2.

2.2 Validation of the Simulation

The first step towards searching for good setup designs for dual-grating interferometers is to find a first reasonable setup parameterization and to validate this numerical finding with experimental measurements.

To this end, a number of parameters are given from the available hardware to build the setup. In detail, the Dual-Phase Grating setup is built with a micro focus tube YXLON Feinfokus FXE-160.99 with a Tungsten transmission target and a focal spot blow 10 µm. The maximum energy is 40 kVp. Lead shielding constrains the source-to-detector distance to a maximum of 1.5 m. The detector model is a Shad-o-Box 6K HS by Teledyne Dalsa with 50 µm pixel pitch and a Gadolinium-Oxysulfid (Gd_2O_2S) converter layer. G_1 and G_1' gratings are made of nickel by the Karlsruhe Nano Micro Facility (KNMF) at the Karlsruhe Institute of Technology and by Microworks GmbH. They have a duty cycle of 50 %, and a height of 8.7 µm, leading to a π-shift at 25 kV. The G_1 period is 4.12 µm, the G_1' period is 4.37 µm.
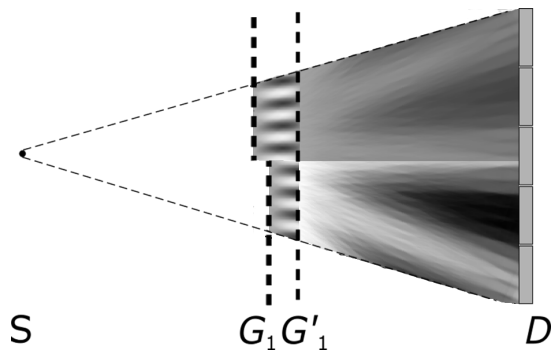
Fig. 3: Intensity patterns from two Dual-Phase Grating setups with different distances between G_1 and G_1'. Both setups create the same envelope period (confer Fig. 2), but result in different visibilities due to the varying G_1 location.

Setup simulations are performed with the CXI package [23]. PSF is modelled as a Gaussian blur with standard deviation (σ) of 74 µm based on prior measurements. Given the above stated grating parameters, we perform an exhaustive search for grating positions that provide the best visibility. In this search, we only consider Moiré periods larger than 200 µm, since smaller periods can not be resolved with the detector resolution and PSF. We report the absolute position of G_1' and the inter-grating distance $d(G_1, G_1')$.

For the setup optimization, fixed grating periods p_1' and p_1 admit two possible distances $d(G_1, G_1')$ that lead to identical envelopes due to the modulus in Eqn. 5 (confer Fig. 2, top). However, it is important to note that although the envelope frequency is identical, the resulting visibilities are in general different. This is illustrated in Fig. 3: If (without loss of generality) the position of G_1' is fixed, the possible positions of G_1 are located at different sections of the underlying Talbot pattern, and thus the visibility of the combined wave is different.

2.3 Modelling G_0 for Dual-Grating Setups

To our knowledge, all existing works on Dual-Phase Grating interferometers are based on micro-focus X-ray tubes. However, for medical applications, it is important to also be able to use brighter X-ray sources, at the expense of a larger focal spot. This requires to validate that the Lau condition [24] for inclusion of a G_0 grating holds also for the Dual-Phase Grating interferometer.

To this end, an ideal G_0 grating is added to the simulation, such that each slit consists of a perfect point source. The period of the grating is adjusted until the wavefronts of the individual sources constructively overlay at the detector plane.

2.4 Dual-Grating Designs for X-ray Tubes with Large Focal Spots

For the experimental setup, it turns out that the required G_0 period is $76.556\,\mu m$, which is a rather atypical G_0 geometry, and would require a rather expensive and time-intensive prototype production.

As a workaround, we perform a second setup parameter search, in which the G_0 period is set fixed to the readily available period of $24.39\,\mu m$, and search for setups with different periods of the easier-to-produce phase gratings. More specifically, we allow for G_1 the realistically producible $0.8\,\mu m$, $0.9\,\mu m$, or $1.2\,\mu m$ gold with $5\,\mu m$ height, which corresponds to a π shift at $25\,keV$. Setup length and X-ray source are identical to the previous experiment, the figure of merit is again the visibility.

The solution space for the distances $\mathrm{d}(S, G_1)$ and $\mathrm{d}(G_1, G_1')$) can be substantially reduced by two constraints. First, the contrast between both phase gratings is highest if the inter-grating distance $\mathrm{d}(G_1, G_1')$ is a fractional Talbot distance. In our case, we directly use the first fractional Talbot distance. Second, $\mathrm{d}(S, G_1)$ is obtained from the Lau condition for the Dual-Phase Grating setup, namely $p_0 = (\mathrm{d}(S, G_1')/\mathrm{d}(G_1, G_1')) \cdot p_1^{\mathrm{proj}}$ (confer Eqn. 7). If p_0 and p_1 are given, the Lau condition relates the missing distances

$$\frac{p_0}{p_1} = \frac{\mathrm{d}(S, G_1')}{\mathrm{d}(G_1, G_1')} \quad . \tag{6}$$

Thus, the only remaining free parameter is the period of the G_1' grating.

3 Results

3.1 Validation of the Simulation

The resulting visibilities from an exhaustive parameter search via simulation are shown in Fig. 4. The x-axis of both plots shows the distance $\mathrm{d}(S, G_1')$. The y-axis shows the period of the envelope. In the left Fig. 4a, the smaller distance $\mathrm{d}(G_1, G_1')$ is used, in the right Fig. 4b the larger distance $\mathrm{d}(G_1, G_1')$. In general, visibilities are higher for a smaller distance $\mathrm{d}(G_1, G_1')$ in Fig. 4a. Sensitivity is somewhat lower for the smaller distance, as it mainly depends on the G_2/G_1' period and the inter-grating distance. However, since the required sensitivity range has to be specifically adapted to a target application to mitigate phase-wraps, it is not a figure of merit in this study. The maximum obtained visibility is about $4.5\,\%$ at an envelope period of $450\,\mu m$, with G_1 period $p_1 = 4.12\,\mu m$, $\mathrm{d}(S, G_1) = 0.473\,m$, G_1' period of $p_1' = 4.37\,\mu m$, and $\mathrm{d}(S, G_1') = 0.5\,m$ at a full setup length of $1.5\,m$. Noise is not modeled in the simulation, such that the experimental visibility is expected to be lower than the simulation.

Experimental measurements with the above stated parameters for a visibility of $4.5\,\%$ are shown in Fig. 5. The fringe visibility is about $2\,\%$. The difference to the simulated visibility can be explained by the lack of noise in

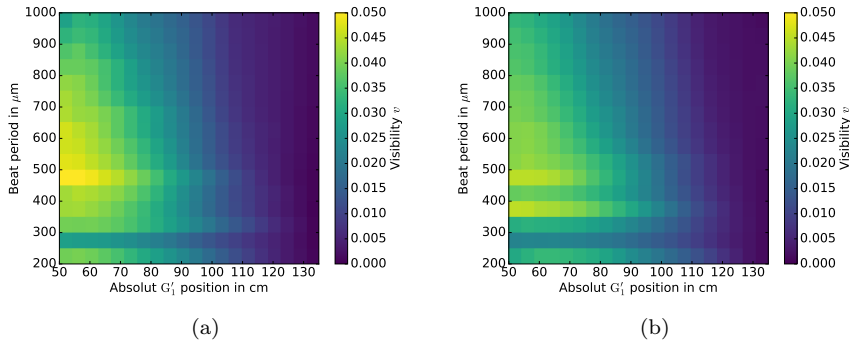(a)   (b)

Fig. 4: Predicted visibilities for different G'_1 positions on the x-axis and different Moiré periods on the y-axis. The intergrating-distances $\mathrm{d}(G_1, G'_1)$ are computed from these values using Eqn. 5 and the setup magnification. (a) visibilities for the smaller inter-grating distances $\mathrm{d}(G_1, G'_1)$. (b) visibilities for the larger inter-grating distances $\mathrm{d}(G_1, G'_1)$.

(a)   (b)   (c)
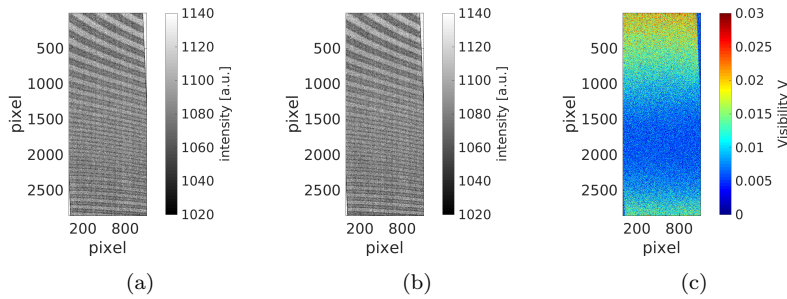
Fig. 5: Experimental fringe pattern and visibility. (a) and (b) show two phase steps. (c) shows a visibility map over the whole grating area.

the simulation (exacerbated by the fact that the used X-ray tube has a relatively low flux), grating and calibration imperfections. The visibility increases at the outer detector parts because the setup design is very compact. Thus, the magnification of the spherical wave is larger in the outer part, leading to a smaller influence of the detector PSF. Overall, simulated experimantal results are sufficiently close for validation.

3.2 Modelling G_0 for Dual-Grating Setups

The same experimental setup is used to determine the equivalent of the Lau condition [24] for a dual-grating setup in simulation. A G_0-source grating is simulated with different periods. The results of multiple constructively overlaid single spot sources are shown in Fig. 6. In Fig. 6 (a), a simulated wave from a single point source is shown. In Fig. 6 (b), overlayed waves from multiple point
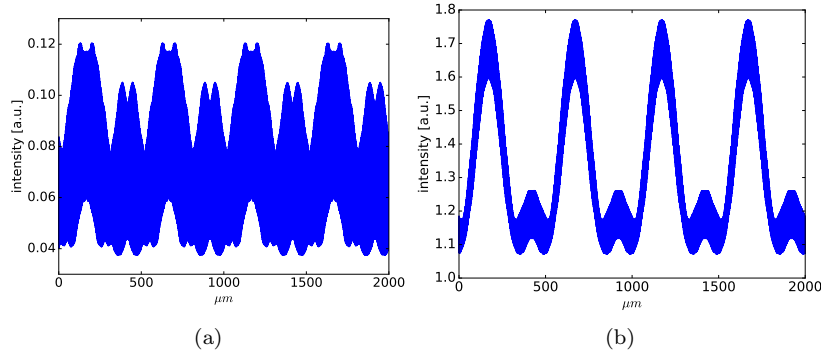
Fig. 6: (a) Example single wavefront created by an ideal point source. (b) multiple waves of ideal spot sources adding up constructively with an optimal G_0 grating (see text for details).

sources from ideal G_0 distances are shown. It can be seen that the unresolvable high-frequency signal of the wave is lost, while the Moiré pattern is preserved. It is confirmed that the optimal G_0 grating period corresponds to the Lau condition for traditional Talbot-Lau interferometers,

$$p_0 = \frac{\mathrm{d}(S, G_1)}{\mathrm{d}(G_1, G_1')} p_1^{\mathrm{proj}} \tag{7}$$

3.3 Dual-Grating Designs for X-ray Tubes with Large Focal Spots

The Lau condition on G_0 is used to constrain the system parameters to the given G_0 grating, and one out of three variants for a G_1 grating. The resulting designs are shown in Table 1. The distances $\mathrm{d}(G_1, G_1')$ between both phase gratings are always between $2\,\mathrm{cm}$ and $5\,\mathrm{cm}$, and the overall setup lengths do not exceed $1.5\,\mathrm{m}$. With these parameters, also the grating periods p_1' are larger then $0.8\,\mathrm{\mu m}$.

#	p_0	$\mathrm{d}(G_0, G_1)$	p_1	$\mathrm{d}(G_1, G_1')$	p_1'	$\mathrm{d}(G_1', D)$	p_b
1	$24.39\,\mathrm{\mu m}$	$0.7884\,\mathrm{m}$	$0.8\,\mathrm{\mu m}$	$0.0267\,\mathrm{m}$	$0.825\,\mathrm{\mu m}$	$0.68\,\mathrm{m}$	$552\,\mathrm{\mu m}$
2	$24.39\,\mathrm{\mu m}$	$0.6653\,\mathrm{m}$	$0.9\,\mathrm{\mu m}$	$0.0255\,\mathrm{m}$	$0.931\,\mathrm{\mu m}$	$0.8039\,\mathrm{m}$	$505\,\mathrm{\mu m}$
3	$24.39\,\mathrm{\mu m}$	$0.887\,\mathrm{m}$	$1.2\,\mathrm{\mu m}$	$0.0459\,\mathrm{m}$	$1.257\,\mathrm{\mu m}$	$0.5671\,\mathrm{m}$	$450\,\mathrm{\mu m}$

Table 1: Parameters of the three newly designed setups.

Table 2 shows the corresponding visibilities v_{micro} that is obtained with a micro focus tube, v_{G_0} that is obtained with a Megalix source with G_0, and v_{ideal} that is obtained with an ideal detector without a PSF.

Exchanging the microfocus tube by a tube with a large focal spot does not significantly penalize the visibilities, as can be seen when comparing v_{micro} with v_{G_0}. Comparing v_{G_0} with v_{ideal} shows that the detector point spread function has a big impact, as it roughly halves the visibilities. We found that a slightly longer propagation distance allows to sample the wavefront more often. This lowers the impact of the PSF and therefore has a positive impact on the visibility. To illustrate this, we also list the visibility $v_{G_0,2.0}$ for a total setup length of $2.0\,\mathrm{m}$.

#	v_{micro}	v_{G_0}	v_{ideal}	$v_{G_0,2.0}$
1	5.2 %	4.5 %	11.66 %	7.3 %
2	11.56 %	9.1 %	19.15 %	11.1 %
3	6.9 %	6.3 %	11.84 %	9.0 %

Table 2: The visibilities of the three systems designed to be operated with available G_0 gratings.

4 Discussion and Outlook

The first Dual-Phase Grating setups proposed by Kagias *et al.* and Miao *et al.* were proof-of-concept systems. In this work, we extend these systems by considering an X-ray tube and detector that are closer to clinical requirements. More specifically, incorporation of the G_0 grating allows to operate the setup with an extended focal spot, and inclusion of the detector model including a non-trivial point spread function allows to model clinically relevant signal loss. We experimentally verified that the Lau condition for incorporating a G_0 grating can be literally transferred to a Dual-Grating-Setup when identifying grating G_1' with grating G_2 of the traditional Talbot-Lau interferometer. Using this condition, we exemplarily search for clinically feasible Dual-Phase Grating designs.

The three systems offer a good tradeoff between the total setup size, the Moiré period at the detector and grating periods. The reached visibilities are in the range of 4.5 to 9.1 % for a setup of $1.5\,\mathrm{m}$ length. These visibilities are lower than typical TLI visibilities. However, the Dual-Phase Grating interferometer benefits from full photon efficiency with no post-~~patient~~ sample attenuation, which partially compensates the lower visibility.

The point spread function considerably reduces the visibility. Thus, a big improvement in the visibility can be expected if CsI(Tl) or modern photon counting detectors with a very narrow PSF are used [25,26]. The visibility can be further improved by optimizing for a somewhat higher frequency envelope. One great advantage of the Dual-Phase Grating interferometer is that the distance between G_1' and the detector is independent of the remaining setup design. For example, the distance can be easily extended by $0.5\,\mathrm{m}$ to a total

setup length of 2 m. The increased visibility can be seen in the last column of Table 2.

The current work is only optimized for duty cycles of 0.5. Rieger *et al.* showed that in classical TLIs, a great improvement can be gained by varying the G_1 duty cycle [27]. In future work, we will investigate whether and how this insight translates to the Dual-Phase Grating interferometer. We also plan to implement a Dual-Phase Grating setup for higher energies, which may be one of its main benefits.

Compliance with ethical standards

Funding
Conflict of interest
The authors declare that they have no conflict of interest.
Ethical approval
This article does not contain any studies with human participants or animals performed by any of the authors.
Informed consent
This article does not contain patient data.

References

1. U. Bonse, M. Hart, An x-ray interferometer, Applied Physics Letters **6**(8), 155 (1965)
2. A. Momose, Recent advances in x-ray phase imaging, Japanese Journal of Applied Physics **44**(9R), 6355 (2005)
3. M. Endrizzi, X-ray phase-contrast imaging, Nuclear Instruments and Methods in Physics Research Section A: Accelerators, Spectrometers, Detectors and Associated Equipment **878**, 88 (2018)
4. F. Pfeiffer, T. Weitkamp, O. Bunk, C. David, Phase retrieval and differential phase-contrast imaging with low-brilliance x-ray sources, Nature physics **2**(4), 258 (2006)
5. M. Stampanoni, Z. Wang, T. Thüring, C. David, E. Roessl, M. Trippel, R.A. Kubik-Huch, G. Singer, M.K. Hohl, N. Hauser, The first analysis and clinical evaluation of native breast tissue using differential phase-contrast mammography, Investigative radiology **46**(12), 801 (2011)
6. K. Scherer, L. Birnbacher, K. Willer, M. Chabior, J. Herzen, F. Pfeiffer, Correspondence: Quantitative evaluation of x-ray dark-field images for microcalcification analysis in mammography, Nature communications **7**, 10863 (2016)
7. K. Hellbach, E. Beller, A. Schindler, F. Schoeppe, N. Hesse, A. Baumann, R. Schinner, S. Auweter, C. Hauke, M. Radicke, F.G. Meinel, Improved detection of foreign bodies on radiographs using x-ray dark-field and phase-contrast imaging., Investigative radiology (2018)
8. D. Stutman, T.J. Beck, J.A. Carrino, C.O. Bingham, Talbot phase-contrast x-ray imaging for the small joints of the hand, Physics in Medicine and Biology **56**(17), 5697 (2011)
9. K. Hellbach, A. Yaroshenko, F.G. Meinel, A.Ö. Yildirim, T.M. Conlon, M. Bech, M. Mueller, A. Velroyen, M. Notohamiprodjo, F. Bamberg, S. Auweter, M. Reiser, O. Eickelberg, F. Pfeifer, In vivo dark-field radiography for early diagnosis and staging of pulmonary emphysema, Investigative radiology **50**(7), 430 (2015)

10. A. Yaroshenko, K. Hellbach, A.Ö. Yildirim, T.M. Conlon, I.E. Fernandez, M. Bech, A. Velroyen, F.G. Meinel, S. Auweter, M. Reiser, O. Eickelberg, F. Pfeifer, Improved in vivo assessment of pulmonary fibrosis in mice using x-ray dark-field radiography, Scientific Reports **5**, 17492 (2015)

11. K. Scherer, A. Yaroshenko, D.A. Bölükbas, L.B. Gromann, K. Hellbach, F.G. Meinel, M. Braunagel, J. Von Berg, O. Eickelberg, M.F. Reiser, F. Pfeifer, S. Meiners, J. Herzen, X-ray dark-field radiography-in-vivo diagnosis of lung cancer in mice, Scientific reports **7**(1), 402 (2017)

12. M. Kagias, Z. Wang, V.A. Guzenko, C. David, M. Stampanoni, K. Jefimovs, Fabrication of au gratings by seedless electroplating for x-ray grating interferometry, Materials Science in Semiconductor Processing (2018)

13. M. Ruiz-Yaniz, F. Koch, I. Zanette, A. Rack, P. Meyer, D. Kunka, A. Hipp, J. Mohr, F. Pfeiffer, X-ray grating interferometry at photon energies over 180 kev, Applied Physics Letters **106**(15), 151105 (2015)

14. A. Sarapata, M. Willner, M. Walter, T. Duttenhofer, K. Kaiser, P. Meyer, C. Braun, A. Fingerle, P.B. Noël, F. Pfeiffer, J. Herzen, Quantitative imaging using high-energy x-ray phase-contrast ct with a 70 kvp polychromatic x-ray spectrum, Opt. Express **23**(1), 523 (2015). DOI 10.1364/OE.23.000523. URL http://www.opticsexpress.org/abstract.cfm?URI=oe-23-1-523

15. T. Thüring, M. Abis, Z. Wang, C. David, M. Stampanoni, X-ray phase-contrast imaging at 100 kev on a conventional source, Scientific reports **4**, 5198 (2014)

16. H. Miao, A. Panna, A.A. Gomella, E.E. Bennett, S. Znati, L. Chen, H. Wen, A universal moiré effect and application in X-ray phase-contrast imaging, Nature Physics **12**, 830 (2016). DOI 10.1038/NPHYS3734

17. M. Kagias, Z. Wang, K. Jefimovs, M. Stampanoni, Dual phase grating interferometer for tunable dark-field sensitivity, Applied Physics Letters **110**(1), 014105 (2017). DOI 10.1063/1.4973520. URL http://aip.scitation.org/doi/10.1063/1.4973520

18. J. Bopp, M. Gallersdörfer, V. Ludwig, M. Seifert, A. Maier, G. Anton, C. Riess, Phasenkontrast röntgen mit 2 phasengittern und medizinisch relevanten detektoren, Bildverarbeitung für die Medizin p. 170 (2018)

19. J. Bopp, V. Ludwig, M. Gallersdörfer, M. Seifert, G. Pelzer, A. Maier, G. Anton, C. Riess, in *Medical Imaging 2018: Physics of Medical Imaging*, vol. 10573 (International Society for Optics and Photonics, 2018), vol. 10573, p. 1057321

20. H.F. Talbot, Lxxvi. facts relating to optical science. no. iv, The London and Edinburgh philosophical magazine and journal of science **9**(56), 401 (1836)

21. M. Takeda, H. Ina, S. Kobayashi, Fourier-transform method of fringe-pattern analysis for computer-based topography and interferometry, JosA **72**(1), 156 (1982)

22. N. Bevins, J. Zambelli, K. Li, Z. Qi, G.H. Chen, Multicontrast x-ray computed tomography imaging using talbot-lau interferometry without phase stepping, Medical physics **39**(1), 424 (2012)

23. A. Ritter, P. Bartl, F. Bayer, K.C. Gödel, W. Haas, T. Michel, G. Pelzer, J. Rieger, T. Weber, A. Zang, G. Anton, Simulation framework for coherent and incoherent x-ray imaging and its application in talbot-lau dark-field imaging, Optics express **22**(19), 23276 (2014)

24. J. Jahns, A. W. Lohmann, The Lau effect (a diffraction experiment with incoherent illumination), Optics Communications **28**(3), p. 263–267 (1979)

25. S.R. Miller, V. Gaysinskiy, I. Shestakova, V.V. Nagarkar, in *Penetrating Radiation Systems and Applications VII*, vol. 5923 (International Society for Optics and Photonics, 2005), vol. 5923, p. 59230F

26. J. Dudak, J. Zemlicka, J. Karch, Z. Hermanova, J. Kvacek, F. Krejci, Microtomography with photon counting detectors: improving the quality of tomographic reconstruction by voxel-space oversampling, Journal of Instrumentation **12**(01), C01060 (2017)

27. J. Rieger, P. Meyer, G. Pelzer, T. Weber, T. Michel, J. Mohr, G. Anton, Designing the phase grating for talbot-lau phase-contrast imaging systems: a simulation and experiment study, Optics Express **24**(12), 13357 (2016)